

The Unusual Late-Time Evolution of the Tidal Disruption Event ASASSN-15oi

T. W.-S. Holoien,^{1*} J. S. Brown,² K. Auchettl,^{3,4} C. S. Kochanek,^{2,3}
J. L. Prieto,^{5,6} B. J. Shappee,⁷ J. Van Saders⁷

¹ *The Observatories of the Carnegie Institution for Science, 813 Santa Barbara St., Pasadena, CA 91101, USA*

² *Department of Astronomy, The Ohio State University, 140 West 18th Avenue, Columbus, OH 43210, USA*

³ *Center for Cosmology and Astro-Particle Physics, The Ohio State University, 191 West Woodruff Avenue, Columbus, OH 43210, USA*

⁴ *Department of Physics, The Ohio State University, 191 W. Woodruff Avenue, Columbus, OH 43210, USA*

⁵ *Núcleo de Astronomía de la Facultad de Ingeniería, Universidad Diego Portales, Av. Ejército 441, Santiago, Chile*

⁶ *Millennium Institute of Astrophysics, Santiago, Chile*

⁷ *Institute for Astronomy, University of Hawai'i, 2680 Woodlawn Drive, Honolulu, HI 96822, USA*

Accepted in MNRAS, 480, 5869.

ABSTRACT

We present late-time optical spectroscopy and X-ray, UV, and optical photometry of the nearby ($d = 214$ Mpc, $z = 0.0479$) tidal disruption event (TDE) ASASSN-15oi. The optical spectra span 450 days after discovery and show little remaining transient emission or evolution after roughly 3 months. In contrast, the *Swift* and *XMM-Newton* observations indicate the presence of evolving X-ray emission and lingering thermal UV emission that is still present 600 days after discovery. The thermal component of the X-ray emission shows a unique, slow brightening by roughly an order of magnitude to become the dominant source of emission from the TDE at later times, while the hard component of the X-ray emission remains weak and relatively constant throughout the flare. The TDE radiated $(1.32 \pm 0.06) \times 10^{51}$ ergs across all wavelengths, and the UV and optical emission is consistent with a power law decline and potentially indicative of a late-time shift in the power-law index that could be caused by a transition in the dominant emission mechanism.

Key words: accretion, accretion disks – black hole physics – galaxies: nuclei

1 INTRODUCTION

When a star passes within the tidal radius of a supermassive black hole (SMBH), the tidal shear forces overwhelm the self-gravity of the star, tearing it apart. If the star is on an approximately parabolic orbit, roughly half of the stellar material will be ejected, while the other half will remain bound and return to pericenter at a rate proportional to $t^{-5/3}$, resulting in a luminous accretion flare (Rees 1988; Evans & Kochanek 1989; Phinney 1989). These tidal disruption events (TDEs) exhibit a wide range of observational properties that depend on many factors, including the physical properties of the disrupted star (e.g., MacLeod et al. 2012; Kochanek 2016), the post-disruption evolution of the accretion stream (e.g., Kochanek 1994; Strubbe & Quataert 2009; Guillochon & Ramirez-Ruiz 2013; Hayasaki, Stone & Loeb 2013, 2016; Piran et al. 2015; Shiokawa et al. 2015), and complex radiative transfer effects (e.g., Gaskell & Rojas

Lobos 2014; Strubbe & Murray 2015; Roth et al. 2016; Roth & Kasen 2018).

If we want to fully understand the observational characteristics and physical properties of these highly energetic events, a large sample of well-studied TDEs is required. While the number of well-studied TDE candidates is growing (e.g., van Velzen et al. 2011; Cenko et al. 2012; Gezari et al. 2012; Arcavi et al. 2014; Chornock et al. 2014; Holoien et al. 2014; Gezari et al. 2015; Vinkó et al. 2015; Holoien et al. 2016b,a; Brown et al. 2016; Blagorodnova et al. 2017; Brown et al. 2017, 2018; Hung et al. 2017), these candidates show a surprising diversity in observed properties, and the number of TDEs that have been well studied at very early and very late times remains quite small.

ASASSN-15oi is a nearby ($d = 214$ Mpc, $z = 0.0479$) TDE discovered by the All-Sky Automated Survey for SuperNovae (ASAS-SN; Shappee et al. 2014) on 2015 August 14 (Brimacombe et al. 2015). We began an immediate follow-up campaign, observing ASASSN-15oi for roughly 3.5 months after discovery using a wide range of both ground

*E-mail: tholoien@carnegiescience.edu

Table 1. Archival Host Galaxy Magnitudes

Filter	Magnitude	Magnitude Uncertainty
<i>NUV</i>	>22.98	—
<i>g</i>	17.66	0.01
<i>r</i>	16.95	0.02
<i>i</i>	16.64	0.01
<i>z</i>	16.45	0.01
<i>J</i>	16.07	0.07
<i>H</i>	15.89	0.07
<i>K_S</i>	15.89	0.09
<i>W1</i>	16.88	0.03
<i>W2</i>	17.46	0.05

Archival magnitudes of the host galaxy from GALEX (*NUV*), Pan-STARRS (*griz*), 2MASS (*JHK_S*) and WISE (*W1 W2*) that were used for fitting the host galaxy SED. The GALEX *NUV* limit is a 3- σ upper limit measured from co-added exposures totaling ~ 200 s of exposure time. The Pan-STARRS magnitudes are Kron magnitudes from the Pan-STARRS Data Release 1 catalog (Flewelling et al. 2016), the 2MASS magnitudes are 5''-radius aperture magnitudes, and the WISE *W1* and *W2* are PSF photometry magnitudes from the AllWISE source catalog. All magnitudes are presented in the AB system.

and space-based observatories (Holoien et al. 2016a). These observations showed that ASASSN-15oi had spectral features resembling the ‘‘Helium-rich’’ TDEs from Arcavi et al. (2014) and optical/UV evolution that was consistent with that of a blackbody and a luminosity declining at a rate best-fit by an exponential profile (though a power-law profile was also a reasonable fit to the data). Interestingly, while the spectral features had faded almost completely only ~ 3 months after discovery, the UV emission remained brighter than the host for the entire period of observations presented in Holoien et al. (2016a).

As was the case with the TDE ASASSN-14li (Holoien et al. 2016b; Brown et al. 2017), we detected soft X-ray emission from ASASSN-15oi during our initial follow-up campaign. However, ASASSN-15oi exhibits much weaker emission than ASASSN-14li, and the detected flux was below an archival upper limit from the ROSAT All-Sky Survey (Voges et al. 1999), making it difficult to ascertain the source of the X-rays, particularly since the flux displayed little evolution during our initial follow-up observations.

Recently Gezari, Cenko & Arcavi (2017) presented UV, optical, and X-ray observations obtained with the *Swift* UltraViolet and Optical Telescope (UVOT; Roming et al. 2005) and X-ray Telescope (XRT; Burrows et al. 2005) and the *XMM-Newton* Observatory, finding that the X-ray emission from ASASSN-15oi exhibited a delayed brightening roughly a year after discovery. This behavior is unique among optically discovered TDEs that emit X-rays, and Gezari, Cenko & Arcavi (2017) argue that the timescale of the brightening suggests that the X-ray emission may be coming from inefficient circularization of the stellar debris stream, resulting in delayed accretion.

In this manuscript we present extended observations of ASASSN-15oi going out to ~ 600 days after discovery, including late-time optical spectra taken with the Inamori-Magellan Areal Camera and Spectrograph (IMACS; Dressler et al. 2011) on the 6.5-meter Magellan-Baade telescope. We also present additional analysis of the extensive UV, optical, and X-ray observations from *Swift* and *XMM-Newton*.

Table 2. Synthetic Host Galaxy Magnitudes

Filter	Magnitude	Magnitude Uncertainty
<i>UVW2</i>	23.32	0.11
<i>UVM2</i>	22.99	0.17
<i>UVW1</i>	21.63	0.09
<i>UVOT</i>	19.52	0.04
<i>B_{UVOT}</i>	18.18	0.03
<i>B_{LCO}</i>	18.13	0.03
<i>V_{UVOT}</i>	17.31	0.02
<i>V_{LCO}</i>	17.26	0.02
<i>I</i>	16.54	0.01

Median synthesized host magnitudes of the host galaxy in the *Swift* UVOT and Las Cumbres Observatory *BVI* filters and their 68% confidence intervals. Magnitudes were synthesized using the process described in §2.1 and are presented in the AB system.

In Section 2 we describe our observations obtained during this extended monitoring campaign. In Section 3 we analyze these data and model the late-time evolution of ASASSN-15oi. Finally, in Section 4 we summarize our results and discuss the implications for future studies of TDEs.

2 OBSERVATIONS

This section summarizes the optical, UV, and X-ray observations taken during our ~ 600 day follow-up campaign of ASASSN-15oi.

2.1 Re-examination of the Host Galaxy 2MASX J20390918-3045201

Since the publication of Holoien et al. (2016a), Pan-STARRS (Chambers et al. 2016; Flewelling et al. 2016) imaging data of the host galaxy 2MASX J20390918-3045201 have become available and provide critical pre-explosion optical fluxes for the galaxy. In this Section we present an updated analysis of the host galaxy 2MASX J20390918-3045201 that incorporates archival observations from the Galaxy Evolution Explorer (GALEX), Pan-STARRS, the Two-Micron All Sky Survey (2MASS; Skrutskie et al. 2006), and the Wide-field Infrared Survey Explorer (WISE; Wright et al. 2010). The archival magnitude measurements used for this fit are shown in Table 1.

We used the publicly available Fitting and Assessment of Synthetic Templates (FAST; Kriek et al. 2009) to fit the spectral energy distribution (SED) of the host galaxy. We assumed a Cardelli, Clayton & Mathis (1989) extinction law with $R_V = 3.1$ and a Galactic extinction of $A_V = 0.19$ mag (Schlafly & Finkbeiner 2011). We employed an exponentially declining star-formation history, a Salpeter initial mass function, and the Bruzual & Charlot (2003) stellar population models. The physical parameters of the host galaxy are largely consistent with our previous results: $M_\star = 1.0^{+0.2}_{-0.1} \times 10^{10} M_\odot$, age = $2.2^{+0.8}_{-0.3}$ Gyr, and a star formation rate $\text{SFR} \leq 0.002 M_\odot \text{ yr}^{-1}$. Our late-time, high signal-to-noise spectra obtained with IMACS are consistent with these properties. In particular, there is no evidence for any nebular emission features that would be indicative of star formation activity.

With the improved constraints on the SED of the host

Table 3. ASASSN-15oi X-ray properties.

Observation	MJD s	Exposure	kT keV	Γ	Blackbody	Unabs. flux	Unabs. flux
		Time ks			Radius 10^{12} cm	of blackbody 10^{-13} erg cm $^{-2}$ s $^{-1}$	of powerlaw 10^{-14} erg cm $^{-2}$ s $^{-1}$
Swift 001-012	57275.1	24.5	0.036 \pm 0.01	1.14 $^{+1.9}_{-1.1}$	1.33 \pm 0.73	1.1 $^{+0.6}_{-0.6}$	1.6 $^{+1.3}_{-1.3}$
XMM 0722160501	57324.6	12.4	0.062 \pm 0.06	1.68 $^{+1.0}_{-0.8}$	0.47 \pm 0.60	1.2 $^{+0.5}_{-0.5}$	2.3 $^{+0.8}_{-0.8}$
Swift 013-027	57325.2	36.4	0.058 \pm 0.01	1.49 $^{+1.9}_{-1.4}$	0.47 \pm 0.16	0.8 $^{+0.3}_{-0.3}$	1.6 $^{+1.2}_{-1.2}$
Swift 028-031	57474.6	12.9	0.047 \pm 0.01	...	2.03 \pm 0.70	6.8 $^{+1.6}_{-1.6}$	< 9.1
XMM 0722160701	57482.7	14.0	0.053 \pm 0.02	2.78 $^{+2.6}_{-1.2}$	1.08 \pm 0.82	3.2 $^{+0.9}_{-1.0}$	1.5 $^{+0.8}_{-0.8}$
Swift 032-045	57545.1	27.4	0.049 \pm 0.01	...	2.01 \pm 0.57	8.2 $^{+1.4}_{-1.1}$	< 8.1
Swift 046-050	57607.4	3.9	0.047 \pm 0.02	1.88 $^{+3.6}_{-1.0}$	2.27 \pm 1.94	8.6 $^{+3.3}_{-3.3}$	9.0 $^{+7.0}_{-1.4}$
Swift 052-053	57839.3	4.1	0.086 \pm 0.08	...	0.23 \pm 0.46	1.0 $^{+0.9}_{-0.9}$	< 87

X-ray properties of ASASSN-15oi measured from the *Swift* XRT and *XMM-Newton* observations. *Swift* data were binned in time to increase the signal-to-noise of the observations; epochs combined in each bin are indicated in Column 1 and total exposure time is given in Column 3.

galaxy, we re-derived the synthetic host magnitudes for each photometric band in our follow-up campaign. In order to determine a robust estimate of the host SED (and uncertainties) we generated 1000 realizations of the archival fluxes, perturbed by their respective uncertainties and assuming Gaussian errors. We then modeled each realization and computed the synthetic magnitudes for each resulting SED. For each filter this yields a distribution of synthetic magnitudes; we report the median and 68% confidence intervals on the host magnitudes in Table 2.

The host magnitudes differ slightly from those derived in our initial analysis; most importantly, we find the host to be roughly 0.1 magnitudes fainter in the *Swift* UV filters than previously estimated. Given the luminosity of the flare, this has little impact on the early-time properties of the flare, but the improved constraints on the host galaxy are crucial for properly interpreting the nature of the flare at later times when the flare has faded considerably.

2.2 Spectroscopic Observations

In addition to the spectra presented in [Holoien et al. \(2016a\)](#), which spanned from 2015 August 21 and 2015 November 7, we obtained low-resolution optical spectra of ASASSN-15oi with IMACS on the Magellan Baade 6.5m telescope and with the Wide-Field Reimaging CCD camera and spectrograph (WFCCD) on the du Pont 2.5m telescope at Las Campanas Observatory in Chile.

The spectra were obtained on UT 2016 Jun. 10.2 (WFCCD, 3×1200 sec), 2016 Aug. 3.1 (IMACS, 5×1450 sec), and 2016 Nov. 6.0 (IMACS, 2×1200 sec) using a $0''.7$ slit and the 300 l/mm grism with f/2 camera on IMACS and $1''.7$ slit with 400 l/mm blue grism on WFCCD which yielded spectra with a spectral resolution of $R = 700 - 1300$. We reduced and extracted the spectra using standard routines in IRAF, including bias subtraction, flat fielding and 1D spectral extraction. The spectra were calibrated in wavelength using HeNeAr lamps obtained at the time of the science exposures and the flux calibration was obtained using the observation of a spectrophotometric standard observed the same night. We discuss the spectral evolution of ASASSN-15oi in Section 3.1.

2.3 Swift Observations

We also obtained and analyzed additional publicly available data from *Swift* from 2016 March 21 through 2017 April 2 (*Swift* target ID 33999; PIs: Hallefors, Horesh, Holoien, Cenko, Gezari). The UVOT observations were obtained in the *V* (5468 Å), *B* (4392 Å), *U* (3465 Å), *UVW1* (2600 Å), *UVM2* (2246 Å), and *UVW2* (1928 Å) filters ([Poole et al. 2008](#)). As in [Holoien et al. \(2016a\)](#), we used the UVOT software task UVOTSOURCE to extract the source counts from a $5''.0$ radius region and a sky region with a radius of $\sim 40''$. The UVOT count rates were converted into magnitudes and fluxes based on the most recent UVOT calibration ([Poole et al. 2008](#); [Breeveld et al. 2010](#)). We present the UVOT magnitudes in Table A1.

In addition to the UVOT observations, ASASSN-15oi was also observed using the photon counting mode of the *Swift* XRT. All observations were reprocessed from level one XRT data using the *Swift* XRTPIPELINE version 0.13.2 script, as suggested in the *Swift* XRT data reduction guide¹. Due to a bright X-ray source ~ 40 arcsec away from the position of ASASSN-15oi, we used a source region centered on the position of ASASSN-15oi with a radius of $20''.0$, and a source free-background region centered at $(\alpha, \delta) = (20:39:25.2, -30:45:26.2)$ with a radius of $110''.0$ to extract the count rate of this event. All extracted count rates were corrected for the fact that our source region encloses only a fraction of the total number of counts arising from the source. Here, the $20''.0$ radius encloses 80% of the flux from the source ([Moretti et al. 2004](#)). We also find that none of our observation suffer from pileup issues.

To increase the signal-to-noise of our observations, we also combined the *Swift* observations into six time bins using XSELECT version 2.4d. From these merged observations, we used the task XRTPRODUCTS version 0.4.2 to extract both source and background spectra using the same regions used to extract our count rates. To generate ancillary response files for each spectra, we used the task XRTMKARF and the exposure maps of each observation produced by the XRTPIPELINE and merged them using XIMAGE version 4.5.1. The response matrix files are ready-made files which were obtained from the CALDB.

¹ http://swift.gsfc.nasa.gov/analysis/xrt_swguide_v1_2.pdf

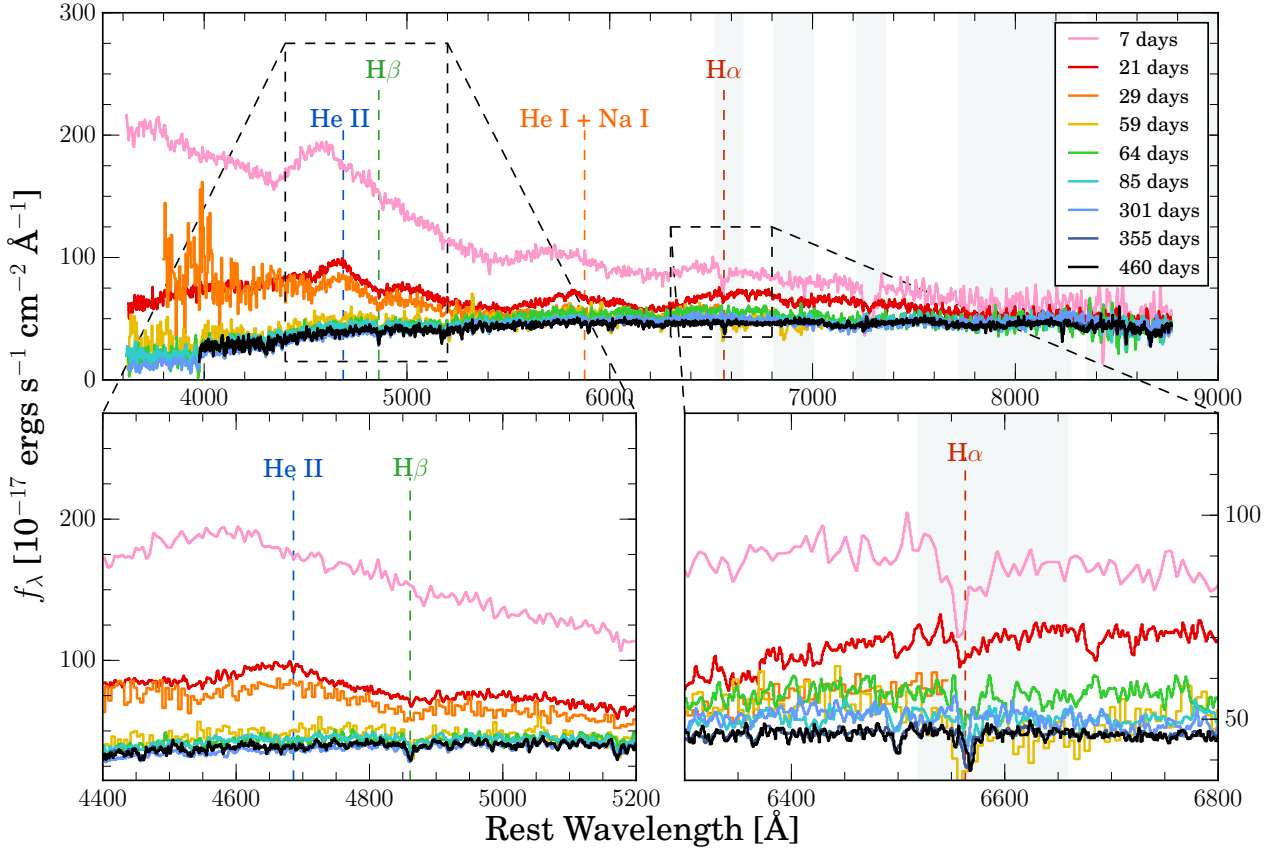


Figure 1. The evolution of the optical spectra of ASASSN-15oi beginning 7 days after discovery (pink) and ending 460 days after discovery (black). The top panel shows the full optical spectra, while the bottom panels show expanded views of the regions around He II $\lambda 4686$ (left) and H α (right). Prominent spectral features commonly observed in TDEs are labeled, and regions prone to systematic errors related to telluric correction are indicated by the shaded bands.

2.4 XMM-Newton Observations

ASASSN-15oi was observed with both the MOS and PN detectors on the *XMM-Newton* Observatory on 2015 October 29 and 2016 April 4 for a total of 16 ks each (ObsID: 0722160501 and 0722160701, PI: Gezari). Both detectors were operated in the full frame mode using a thin filter, however we use only the PN detector for our study due to its high sensitivity, and large effective area. All data reduction and analysis was done using the *XMM-Newton* science system (SAS) version 15.0.0² with CALDB 4.6.8³.

We first checked for periods of high background and/or proton flares by generating a count rate histogram using events with energy between 10–12 keV. We find that these observations are only slightly affected by high background or flares, giving effective exposure times in the PN detector of ~ 11 ks and ~ 13 ks for 0722160501 and 0722160701, respectively. We reduced the data following the standard screening of events, with single and double events (PATTERN ≤ 4) selected for the PN detector. We also used the standard set of FLAGS for the PN (#XMMEA_EP) detector. We also corrected for vignetting by processing all event

files using the task EVIGWEIGHT⁴. We extracted the spectrum of ASASSN-15oi using the SAS task EVSELECT and the cleaned, vignetting-corrected event files from the PN detector using the same source and background region that we used for the *Swift* observations. Count rates are also extracted from the PN observations using the same regions and corrected for the encircled energy fraction⁵. These data are analyzed in Section 3.3 and Section 3.2.

3 EVOLUTION OF THE LATE-TIME EMISSION

In this section we discuss the optical, UV, and X-ray evolution of ASASSN-15oi and interpret the physical conditions of the system.

3.1 Evolution of the Optical Spectra

In Holoien et al. (2016a) we presented spectra spanning the first 85 days after the discovery of ASASSN-15oi, noting

² <https://www.cosmos.esa.int/web/xmm-newton/documentation/>

³ <https://www.cosmos.esa.int/web/xmm-newton/calibration>

⁴ See <https://xmm-tools.cosmos.esa.int/external/sas/current/doc/evigweight> for more details

⁵ <https://heasarc.nasa.gov/docs/xmm/uhb/onaxisraysf.html>

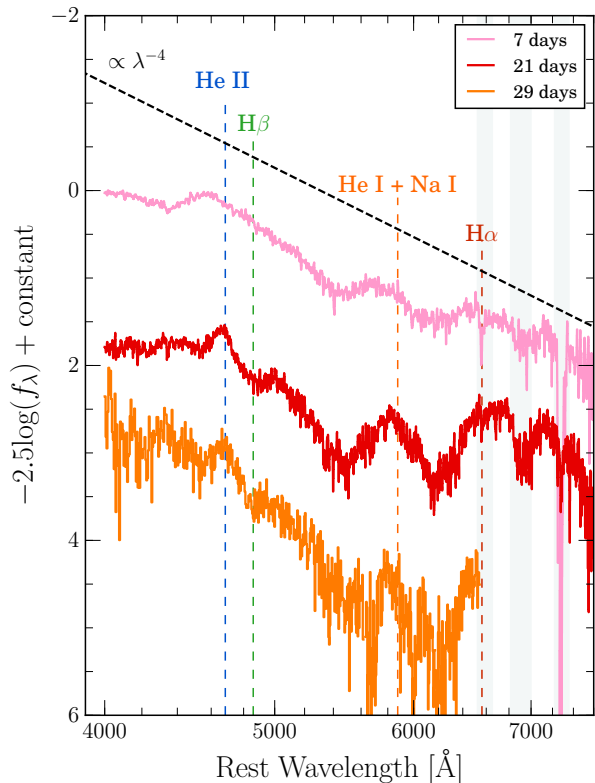


Figure 2. Host-subtracted early time spectra. The color scheme is the same as Figure 1, and the same prominent TDE emission features are labeled. Note that the absorption feature near $H\alpha$ is due to telluric absorption. The flare continuum is reasonably approximated by the Rayleigh-Jeans tail of a blackbody; the host subtracted spectra clearly show the early-time evolution of the emission features.

that the TDE exhibited a strong blue continuum and broad helium line emission but little-to-no hydrogen emission features in its spectra. The spectra most closely matched those of the “He-rich” events from Arcavi et al. (2014), such as PS1-10jh and PTF09ge (Gezari et al. 2012; Arcavi et al. 2014). As was the case with ASASSN-14ae and ASASSN-14li, the blue continuum weakened and the emission lines became narrower and weakened over time, but unlike the other ASAS-SN TDEs, the transient emission features seemed to fade completely from the spectra within roughly 2 months after discovery.

Figure 1 shows the evolution of the optical spectra of ASASSN-15oi beginning 7 days after discovery (pink) and ending 460 days after discovery (black). The top panel shows the full optical spectra, while the bottom panels show expanded views of the regions around $He II \lambda 4686$ (left) and $H\alpha$ (right). After the initial ~ 2 months, there is surprisingly little evidence of any TDE signatures whatsoever. In the absence of any archival spectra, this was not immediately clear when we initially analyzed this object. However, the high signal-to-noise spectra obtained at late-times with IMACS confirm that the late-time spectra are overwhelmingly dominated by the host galaxy light.

In Figure 2 we use the late-time, high signal-to-noise spectrum as a template for the host and subtract it from the early-time flare-dominated spectra. The trends seen in the

Figure 1, in particular the evolution towards lower velocities and narrower lines, are even more pronounced in these host-subtracted spectra. This evolution takes place on a much shorter timescale than most other TDEs (e.g., ASASSN-14ae; Holoien et al. 2014; Brown et al. 2016 and ASASSN-14li; Holoien et al. 2016b; Brown et al. 2017). However, one other nearby TDE, iPTF16fnl, exhibited a similar spectroscopic evolution (Blagorodnova et al. 2017; Brown et al. 2018). Both objects displayed rapidly fading optical spectra, though at early times the emission lines in ASASSN-15oi are much more blueshifted than the lines seen in iPTF16fnl. The host-subtracted spectra also show that the continuum shape is broadly consistent with the Rayleigh-Jeans tail of a blackbody, consistent with the photometric data.

Finally, the host-subtracted spectra make it quite clear that there is likely some $H\alpha$ emission at early times. While the rest frame $H\alpha$ line emission falls within the B-band telluric feature, there is compelling evidence of a broad blue wing associated with $H\alpha$ emission. Within the context of the broader population of the TDEs, ASASSN-15oi remains in the relatively He-rich regime, especially when compared ASASSN-14ae and ASASSN-14li.

3.2 Analysis of the X-ray Emission

To analyze the X-ray spectra of ASASSN-15oi, we used the X-ray spectral fitting package XSPEC version 12.9.1 using chi-squared statistics. Using the FTOOLS command GRPPHA, we group each spectrum from the merged *Swift* observations and the *XMM-Newton* observations with a minimum of 10 counts per energy bin. Early *Swift* observations of ASASSN-15oi showed that the X-ray emission from this event can be well fit using an absorbed blackbody plus power law (Holoien et al. 2016a). As we are interested in how the X-ray emission from the source changes with time, we fit each spectra over an energy range of 0.3–5.0 keV using either an absorbed blackbody model or an absorbed blackbody plus power law model that is emitting at the redshift the TDE. Here, we assume Wilms, Allen & McCray (2000) abundances, and initially fit N_H , the temperature of the blackbody (kT), the power law index (Γ), and the normalization. We find that for nearly all spectra, letting N_H vary does not significantly improve the fit to the data, and thus we fix it to the Galactic HI column density in the direction of ASASSN-15oi, $5.59 \times 10^{20} \text{ cm}^{-2}$ (Kalberla et al. 2005).

Similar to Holoien et al. (2016a), we find that at early times (< 200 days), the X-ray emission of ASASSN-15oi can be well described using an absorbed blackbody plus power law model. At late times (> 200 days) we find that having an additional power law component is not required for all *Swift* epochs. Within the uncertainties, there is little evidence for variation in the power law index when a power law component is detected, however at late times the flux of this component seems to increase slightly when compared to the second XMM observation (see Table 3).

The bulk of the X-ray emission from ASASSN-15oi can be described using a simple absorbed blackbody model. By merging the available *Swift* observations into six time bins we were able to derive the flux of the blackbody component (and the power law component if present) by modeling the X-ray spectrum. Similar to what was found by Gezari, Cenko & Arcavi (2017), Figure 3 shows that the unabsorbed X-ray

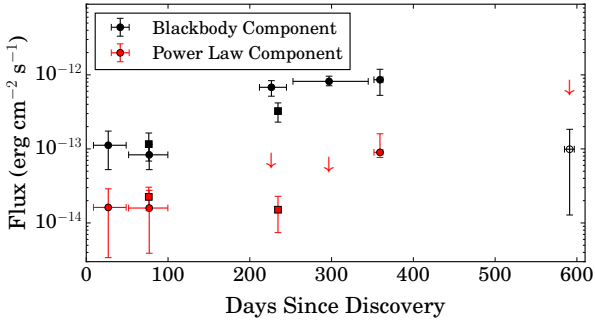


Figure 3. The flux from the blackbody (black points) and power law (red points) components of the X-ray emission. Arrows indicate upper limits on the flux. In epochs where both components are detected, the blackbody flux is roughly an order of magnitude stronger than the power law flux, and the blackbody component shows a significant long-term brightening between ~ 200 and ~ 400 days, while the power law component remains relatively constant.

flux from the blackbody component brightened by a factor of 4–10 between the emission detected at early times (< 200 days) and that detected at late times (> 200 days), despite the temperature of the blackbody component remaining constant (within uncertainties) during this time. This behavior is not seen in other X-ray TDEs over such long timescales. Most of the X-ray TDEs, including ASASSN-15oi, exhibit some variability on short timescales. However, over longer timescales the X-ray emission usually decays following a simple power law (see, e.g., [Auchettl, Guillochon & Ramirez-Ruiz \(2017\)](#) for the long term behavior of X-ray TDEs, or individual studies such as those of ASASSN-14li: [Brown et al. 2017](#) and Swift J1644+57: [Mangano et al. 2016](#) for variability observed over short timescales). This is in contrast with the flux of the power law component, which seems to stay relatively constant with time. [Gezari, Cenko & Arcavi \(2017\)](#) suggested that the unique behavior of the thermal component of this source arises from inefficient circularization, resulting in delayed accretion, though this could also be explained by the material surrounding the accretion disk being optically thick to X-ray radiation at early times before becoming optically thin a few months after discovery (e.g., [Metzger & Stone 2016](#)). The former explanation is more likely in this case as we do not see any significant change in N_H from the X-ray observations.

Previously, we placed strong limits on the presence of an underlying AGN based on a non-detection from archival *ROSAT* all-sky survey data ([Holoien et al. 2016a](#)). However, a re-examination of this calculation discovered that the limit presented in [Holoien et al. \(2016a\)](#) is an order of magnitude higher than actually implied by the non-detection of this source. From our re-examination of the data, we derive an upper limit of 5.8×10^{-2} counts/sec in the 0.3–10.0 keV energy band. Assuming a power law component with $\Gamma = 1.75$, similar to that of known AGN (e.g., [Tozzi et al. 2006](#); [Marchesi et al. 2016](#); [Liu et al. 2017](#); [Ricci et al. 2017](#)), we derive an unabsorbed flux limit of 1.9×10^{-12} ergs cm^{-2} s^{-1} , which corresponds to $L_X \sim 10^{43}$ erg s^{-1} at the distance of the TDE. This is comparable to the observed X-ray luminosities of AGN found in deep extragalactic surveys, so we cannot rule out the presence of an underlying AGN. However, in

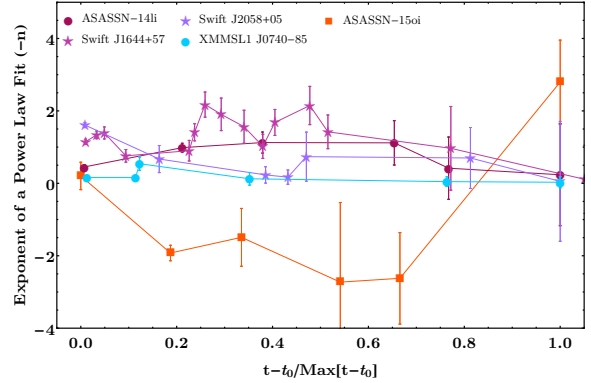


Figure 4. Best-fit exponent of a power law fit ($-n$) and its uncertainty as the time of discovery/peak (t_0) goes to infinity, as a function of $t - t_0$ for ASASSN-15oi (orange squares). Overlaid are the evolution of the jetted events X-ray TDEs Swift J1644+57 and Swift J2058+05 (pink and purple stars, respectively), and the non-jetted X-ray TDEs ASASSN-14li and XMMSL1 J0740-85 (burgundy and cyan circles, respectively) as presented in [Auchettl, Ramirez-Ruiz & Guillochon \(2018\)](#). The power law index of ASASSN-15oi exhibits a similar magnitude of variation to those seen in the other X-ray TDEs, rather than the large-scale variations seen in AGN, though it is of the opposite sign.

[Holoien et al. \(2016a\)](#) we highlighted that the host galaxy has a mid-IR color from WISE of $W_1 - W_2 = 0.06 \pm 0.06$, which implies that any AGN activity in the host galaxy is not strong ([Assef et al. 2013](#)). Further long-term observations are needed to confirm whether the hard component of the X-ray emission is associated with the TDE itself and is possible evidence of a jet, or whether it persists well after the TDE fades, which would imply the presence of an underlying, weak AGN.

In order to investigate the origin of the X-ray emission, we compare properties of the X-ray emission of ASASSN-15oi to those of other X-ray emitting TDEs using the metric presented by [Auchettl, Ramirez-Ruiz & Guillochon \(2018\)](#) to distinguish TDEs from AGN. [Auchettl, Ramirez-Ruiz & Guillochon \(2018\)](#) fit a temporal power law, $f \propto (t - t_0)^{-n}$, to the X-ray emission of several TDEs and AGN and found that TDEs show a relatively coherent decay with $n \sim 0 - 2$, while AGN varied dramatically on short timescales with a much broader range of indices ($-10 < n < 15$). Figure 4 shows $-n$ as a function of time for ASASSN-15oi and several X-ray TDEs from the analysis of [Auchettl, Ramirez-Ruiz & Guillochon \(2018\)](#). While ASASSN-15oi shows a constant power-law exponent, unlike AGN which have n values that vary dramatically over short time-scales, it is unique in that it has a negative value of n , due to its remarkable power-law brightening in the X-rays with time. As such, it is very likely that this thermal component arises from the TDE itself.

In Figure 5 we show the evolution of the hardness ratio (HR) as compared to the “X-ray TDEs” from [Auchettl, Ramirez-Ruiz & Guillochon \(2018\)](#). Similar to what was seen in XMMSL1 J0740-85, the X-ray emission of ASASSN-15oi shows little color evolution with time and is relatively soft. Here we have assumed that the hard X-ray component is not associated with the TDE.

However, if one assumes that the hard X-ray compo-

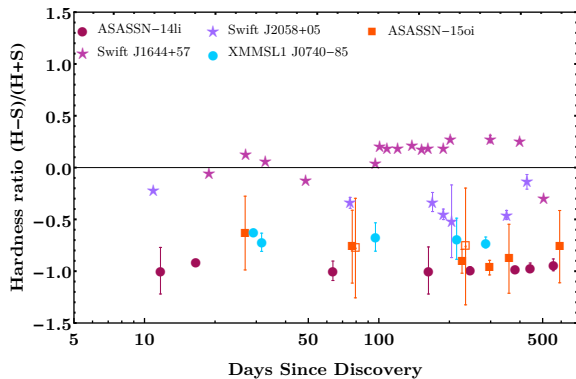


Figure 5. X-ray hardness ratio as a function of time for ASASSN-15oi. Here the hardness ratio derived from the merged *Swift* observations are plotted as filled orange squares, while the ratio derived from the two deep XMM-Newton observations are shown as unfilled orange squares. Overlaid are the hardness ratios for the non-jetted thermal X-ray TDEs (ASASSN-14li and XMMSL1 J0740-85) and the jetted X-ray TDEs (Swift J1644+57, Swift J2058+05), taken from Auchtettl, Guillochon & Ramirez-Ruiz (2017).

ment is associated with the TDE itself, rather than an underlying AGN, ASASSN-15oi would exhibit strong variation in its HR, much larger than that seen from the non-jetted thermal and jetted X-ray TDEs plotted in Figure 5. Under this assumption, we find that the HR derived from XMM-Newton (unfilled squares) would be closer to $HR \sim 0$, rather than $HR \sim -0.7$ presented in the plot. If the hard X-ray component is associated with the TDE itself, in the form of a possible jet, then this variation may be indicative of variations in the accretion rate of this source, assuming that the jet luminosity is related to the accretion rate. However, this variation is much larger than that seen from other X-ray TDEs that exhibit a jet. In addition, this change in HR would be in conflict with the HR derived from the *Swift* observations (filled squares) that were taken nearly simultaneously, which would imply very large variability on a very short timescale. While similarly strong variability on short timescales has been seen in AGN (e.g., Auchtettl, Ramirez-Ruiz & Guillochon 2018), this would be highly unique for a TDE. Irrespective of the origin of the underlying hard X-ray component, this highlights the importance of performing deep observations using high sensitivity X-ray instruments such as XMM-Newton as a complement to those observations taken using *Swift*.

3.3 Photometric Evolution

Figure 6 shows the photometric evolution of ASASSN-15oi in the X-ray, UV, and optical, extending the results from Holoien et al. (2016a) to ~ 600 days after discovery. As in Holoien et al. (2016a), the *Swift* *B*- and *V*-band data were converted to the Johnson-Cousins system to be consistent with data obtained from the Las Cumbres Observatory 1-m telescopes. The colored horizontal dashed lines represent the synthesized host magnitudes in the UV and optical bands, and the horizontal black line shows the X-ray upper limit from ROSAT.

Two main features of the photometric evolution stand out. First, the X-ray emission shows significant evolution at later times, as discussed in §3.2. Second, while the spectral features faded quickly, the UV emission from the TDE leveled off at around 250 days after discovery, and continues to be brighter than the host 600 days after discovery. This is similar to ASASSN-14li, which also had a similar leveling off in its late-time UV emission (Brown et al. 2017). This may indicate a transition in the physical mechanism responsible for the emission.

To characterize this excess UV emission, we corrected the UV and optical magnitudes for Galactic extinction assuming $R_V = 3.1$ and $A_V = 0.19$ (Schlafly & Finkbeiner 2011), deriving the extinction in other filters using a Cardelli, Clayton & Mathis (1989) extinction law. We then subtracted the host flux in each band and modeled the UV and optical SED of ASASSN-15oi as a blackbody using Markov Chain Monte Carlo methods, as was done for the previous ASAS-SN TDEs (Holoien et al. 2014, 2016b; Brown et al. 2016, 2017). When performing the fit, we excluded any data where $f_\lambda/f_{\lambda,host} < 0.5$, as we did in Holoien et al. (2016a). Many of the later epochs of *Swift* observations resulted in non-detections or marginal detections, and in order to increase the significance of our flux measurements we binned the data taken 200 days or more after discovery in 20-day bins. These binned fluxes were used to fit the blackbody SED at late-times, rather than the individual observations. We find that in all epochs the UV and optical emission is well described by a blackbody, although in some cases data was only available in one or two filters.

In Holoien et al. (2016a) we found that when we fit the SED, the fits preferred a rising temperature in early epochs. Because of this, we fit the SED using a fairly restrictive temperature prior: for epochs within 10 days of discovery, the temperature was fit with a prior of $T = 2 \times 10^4$ K, and for later epochs, we fit the data with a prior of $T = (2 + (\Delta t - 10)/2) \times 10^4$ K, where $\Delta t = MJD - 57248.2$ and the temperature is capped at $T = 40000$ K, with a log uncertainty of ± 0.05 dex in all epochs. In the later epochs, the source is becoming redder, indicating a decreasing temperature, so for this manuscript we revised the blackbody fits using a much less restrictive prior of $10000 \text{ K} \leq T \leq 55000 \text{ K}$ in all epochs. Figure 7 shows the blackbody temperature evolution of ASASSN-15oi using this new prior. In the earliest epochs, the temperature is not well-constrained because our *Swift* data do not span the peak of the SED, and we find that the fits prefer to fit values near the higher end of our prior range. However, in the late-time data, the data prefer cooler temperatures of 20000 K–30000 K, indicating that the flare cooled before leveling off.

Figure 7 also shows the temperature evolution of the thermal component of the X-ray data. The X-ray emission from ASASSN-15oi can be well described using a simple blackbody, assuming that the hard X-ray tail is not associated with the TDE. As originally highlighted in Holoien et al. (2016a), the initial temperature evolution of ASASSN-15oi is unique compared to other well-characterized TDEs such as ASASSN-14li (Brown et al. 2017). There is some hint that the X-ray temperature follows a similar behavior to that seen in the UV/optical, with the X-ray temperature initially increasing and then flattening. However, the large uncertainty on the blackbody temperature derived from the

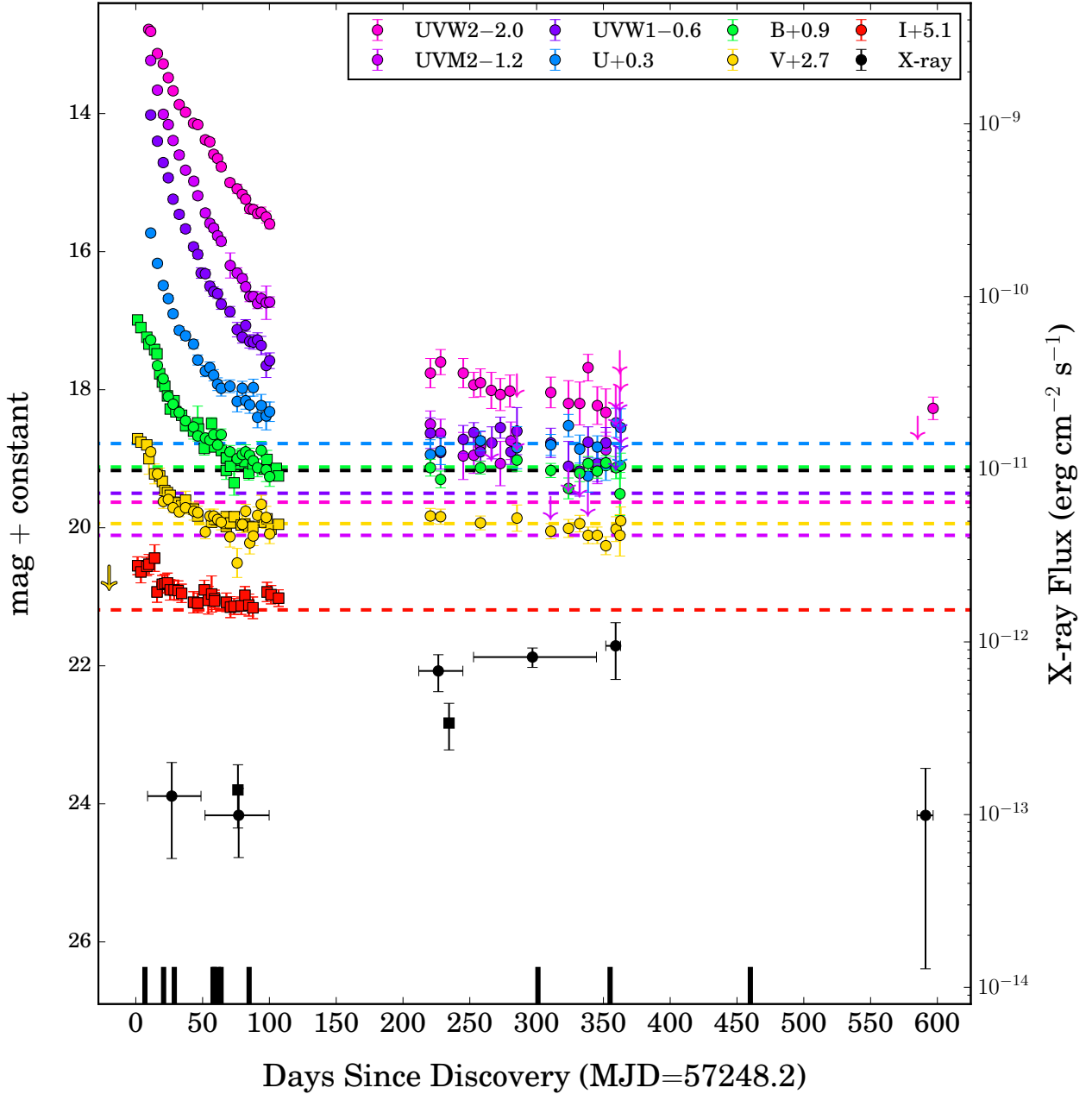


Figure 6. Evolution of ASASSN-15oi in the X-ray, UV, and optical bands from discovery to ~ 600 days after discovery. Follow-up data obtained from *Swift* (X-ray, UV, and optical) are shown as circles and follow-up data obtained by the Las Cumbres Observatory 1-m telescopes (optical) and *XMM-Newton* (X-ray) are shown as squares. Upper limits are indicated with downward arrows, and the *V*-band upper limit at -20 days is a 3σ upper limit from ASAS-SN. All optical and UV magnitudes are on the Vega system (left scale), and unabsorbed X-ray fluxes in the $0.3 - 10.0$ keV energy range are shown in $\text{ergs cm}^{-2} \text{s}^{-1}$ (right scale), and the two scales have the same dynamic range. UV/optical data have not been corrected for Galactic extinction. The XRT data have been binned to increase signal-to-noise of the detections, and horizontal error bars indicate the date range for each bin. Horizontal dashed lines show the synthesized UVOT and *BVI* host magnitudes and the archival X-ray upper limit from ROSAT, and vertical marks along the time-axis show the dates of our spectroscopic observations.

first *XMM-Newton* observation makes it difficult to make strong statements about the initial evolution. In all epochs, the X-ray temperature is an order of magnitude or more hotter than the UV/optical component, suggesting the emission arises from a different region around the SMBH.

Figure 8 shows the UV/optical and X-ray luminosity evolution of ASASSN-15oi. The early observations show a

plateau in the first couple of weeks followed by a steady decline in luminosity, possibly indicating the transient was discovered near its peak luminosity. Conversely, the late-time data indicate that the UV/optical luminosity was approximately constant for the last ~ 400 days of observation. In the Figure we also show $t^{-5/3}$ power-law fits to the early data (dashed lines) and $t^{-5/12}$ power-law fits to the late-

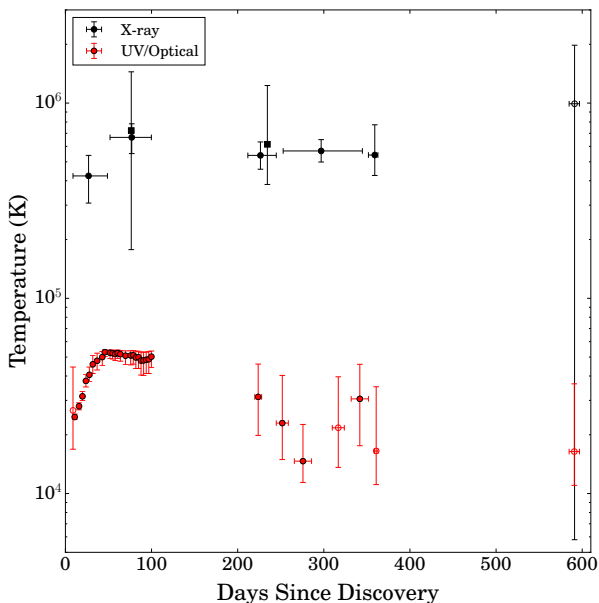


Figure 7. Temperature evolution of ASASSN-15oi from blackbody fits to the UV/optical SED (red points) and of the thermal component of the X-ray emission from *Swift* XRT (black circles) and *XMM-Newton* (black squares). Data obtained more than 200 days after discovery were binned, with the horizontal bars indicating the date range of the observations. Filled circles indicate bins with 3 or more epochs of observation, while open circles have 1 or 2 epochs of observation.

time data (dotted lines). We find that the early data is reasonably well-fit by a $t^{-5/3}$ power-law profile, as we found in [Holoien et al. \(2016a\)](#), but that this profile cannot fit the late-time data. The late-time data are reasonably well-fit by a $t^{-5/12}$ power-law profile, though the best-fit power law index is poorly constrained and highly sensitive to the choice of t_0 . For the late-time fit shown in the Figure, we fix t_0 to the value fit from the early-time data. When the bolometric luminosity is fallback-dominated we expect a $t^{-5/3}$ decline, and when it is dominated by emission from the accretion disk we expect a $t^{-5/12}$ decline ([Lodato & Rossi 2011](#)), though the decline rates in individual UV/optical filters can differ from the bolometric decline rate due to band effects. While the best-fit power laws to the early and late-time data are not exactly $t^{-5/3}$ and $t^{-5/12}$, the differing power law fits indicate that we may be observing a transition from a fallback-dominated regime to a disk-dominated regime, or some other transition in the emission mechanism like that seen in other TDEs (see e.g., [Auchettl, Guillochon & Ramirez-Ruiz 2017](#)).

The combined blackbody-plus-power-law X-ray luminosity is also shown in Figure 8. At early times, the X-ray emission is 2 orders of magnitude or more weaker than the UV/optical emission, but during the period of increased X-ray emission between ~ 200 days and ~ 400 days, the X-rays become the dominant source of emission. The X-ray emission fades again to early-time levels in the last epoch of observation at ~ 600 days, but the UV/optical emission has also faded significantly by that time, and the X-rays and UV/optical make similar contributions to the overall luminosity. Thus, while the X-rays are relatively insignificant at

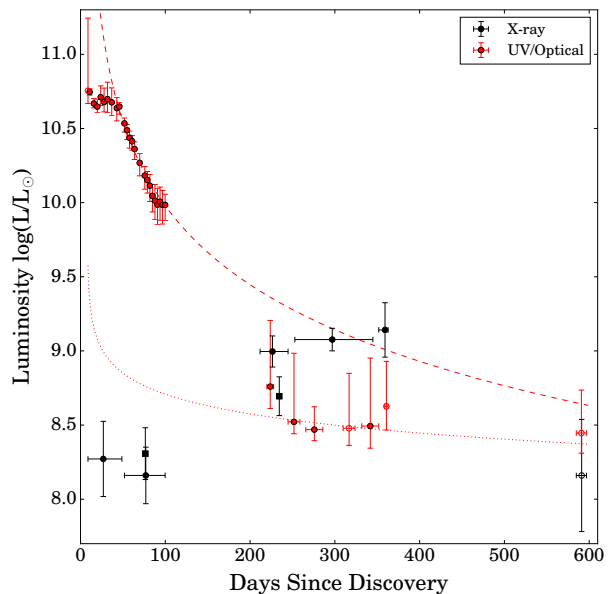


Figure 8. UV/optical luminosity evolution of ASASSN-15oi from the blackbody SED fits (red circles) and X-ray luminosity evolution from *Swift* (black circles) and *XMM-Newton* (black squares). The red dashed line shows a $t^{-5/3}$ power-law fit to the early UV/optical data and the red dotted line shows a $t^{-5/12}$ power-law fit to the late-time UV/optical data. When fitting the late-time data, we fixed the time of disruption t_0 to be the same as that fit from the early data.

early times, they represent a significant or dominant fraction of the energy emitted at later times.

Integrating the combined optical/UV and X-ray luminosity curves gives a total radiated energy of $E = (1.32 \pm 0.06) \times 10^{51}$ ergs for the ~ 600 days of follow-up observations. This required accretion of only $\Delta M \sim 7.4 \times 10^{-3} \eta_{0.1}^{-1} M_{\odot}$ of mass, where $\eta_{0.1} = 0.1\eta$ is the radiative efficiency, to power the event, assuming the flare is powered by accretion. This is similar to the amount of mass needed to power ASASSN-14li, $\Delta M \sim 4 \times 10^{-3} \eta_{0.1}^{-1} M_{\odot}$, as derived by [Brown et al. \(2017\)](#).

The evolution of the effective radius for the UV/optical and X-ray emission are shown in Figure 9. We originally estimated the mass of the SMBH to be $10^{7.1} M_{\odot}$ in [Holoien et al. \(2016a\)](#) using the host galaxy bulge mass and the bulge-black hole mass relation from [McConnell & Ma \(2013\)](#). However, more recently [Gezari, Cenko & Arcavi \(2017\)](#) and [Mockler, Guillochon & Ramirez-Ruiz \(2018\)](#) found that the mass of the SMBH in 2MASX J20390918-3045201 is more likely on the order of $M_h \sim 10^{6.4} M_{\odot}$, using a total stellar mass-black hole mass relation ([Reines & Volonteri 2015](#)) and the Modular Open Source Fitter for Transients fitting code ([Guillochon et al. 2017](#)), respectively. Because of these new, lower mass estimates, we scale the photospheric radii shown in Figure 9 to the gravitational radius of a $10^6 M_{\odot}$ mass black hole.

As was seen with ASASSN-14li ([Brown et al. 2017](#)), the radius implied by the UV/optical emission initially shrinks and then levels off at later times. The blackbody radius of ASASSN-15oi is larger than that of ASASSN-14li early in the flare ($R \sim 10^4$ gravitational radii, compared to $R \sim 10^3$

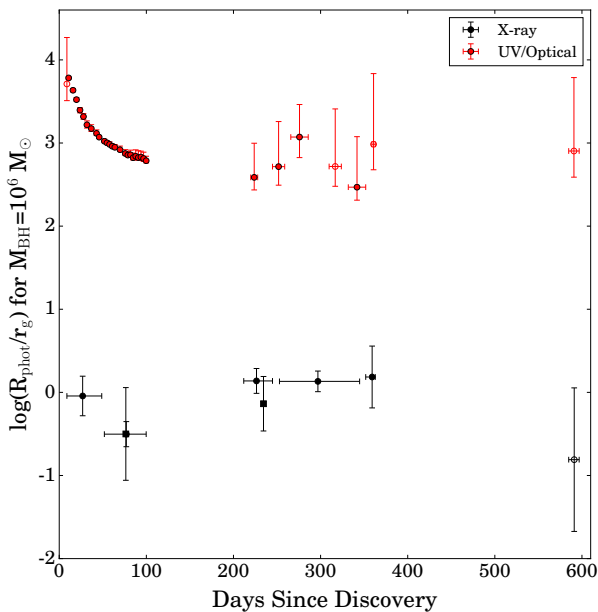


Figure 9. Evolution of the photospheric radius derived from the blackbody SED fits (red circles) and X-ray emission from *Swift* (black circles) and *XMM-Newton* (black squares), shown in units of the gravitational radius of a $10^6 M_{\odot}$ black hole. Similar to what was seen in ASASSN-14li, the size of the UV/optical emitting region shrinks and then levels off at later times, though ASASSN-15oi exhibits a smaller UV/optical photosphere than ASASSN-14li. Conversely, the size of the X-ray emitting region remains relatively constant throughout the event.

gravitational radii for ASASSN-14li), but both TDEs level off at a similar size of roughly 10^3 gravitational radii.

We also show the characteristic radius of the X-ray emission in Figure 9, again assuming that a spherical blackbody well describes the soft X-ray emission. The X-ray emitting surface is approximately 1 gravitational radius in size, again assuming a $10^6 M_{\odot}$ black hole. This is significantly smaller than the characteristic radius of the UV/optical emission from ASASSN-15oi. Unlike the UV/optical emission, we do not see a decrease in the size of the photosphere with time. The size of the X-ray emitting region seems to remain relatively constant, although the uncertainties are fairly large. We also observed little evolution in ASASSN-14li (Brown et al. 2017), and similar to the UV/optical emitting surface, the emitting X-ray surface of ASASSN-15oi is again comparable to that of ASASSN-14li. There is some evidence that the size of the X-ray emitting region increases between 200–400 days, and it is possible the increase in the observed X-ray flux of the blackbody component may be a natural result of this.

4 DISCUSSION

After discovering the nearby TDE ASASSN-15oi and publishing our initial observations in Holoien et al. (2016a), we continued to monitor this object in the optical, UV, and X-rays to roughly 600 days after discovery. Our late-time observations show that while ASASSN-15oi shows many similarities with other TDEs, it is also unique in a number of ways.

Our spectroscopic monitoring program indicates that the spectroscopic features, including the strong blue continuum and emission lines, faded rapidly, and were essentially gone roughly 2 months post-discovery. Such rapid evolution of the spectral features was only seen in one other optically discovered TDE, iPTF16fnl, which was significantly less luminous than ASASSN-15oi (Blagorodnova et al. 2017; Brown et al. 2018). The host-subtracted spectra indicate that the continuum slope is reasonably approximated by the Rayleigh-Jeans tail of a blackbody, and that the emission lines narrow as they fade, as has been seen in other optically discovered TDEs (e.g., Holoien et al. 2014, 2016b; Brown et al. 2016, 2017). The host-subtracted spectra also make it apparent that there is likely a weak $H\alpha$ emission feature, though the helium emission lines are significantly stronger, and thus ASASSN-15oi still falls on the He-rich end of the continuum of spectroscopic features described in Arcavi et al. (2014).

As first reported by Gezari, Cenko & Arcavi (2017) the evolution of the X-ray emission seen in ASASSN-15oi is unique. In particular, the X-ray emission brightens by roughly an order of magnitude by ~ 250 days before fading back to early levels in the latest epochs of observation. Our analyses indicate that the bulk of this evolution comes from the thermal component of the X-rays, and that the hard component, when detected, is weaker and relatively constant throughout the flare. While all the detected X-ray emission is below an archival limit from ROSAT, the X-ray emission evolves without significant short-timescale variations, is relatively soft in nature and shows little variation in hardness ratio with time, consistent with that of other X-ray TDEs (Auchetti, Ramirez-Ruiz & Guillochon 2018). We conclude that the thermal component of the X-ray emission is almost certainly due to the TDE, while the origin of the hard component is still unclear. Though the lack of evolution in the hard component indicates it is likely related to the host, rather than the TDE, further X-ray observations showing that the hard component remains constant are needed to definitively show that this is the case.

The TDE also continues to emit in the UV at 600 days, remaining well above the estimated host flux despite leveling off and showing very little evolution in the late-time observations. This behavior is very similar to that of ASASSN-14li (Brown et al. 2017), but ASASSN-14li also showed long-lasting optical spectroscopic features. ASASSN-15oi shows significant temperature evolution, growing much hotter in early epochs before cooling and remaining constant during the late-time observations. The early luminosity evolution is relatively well-fit by a $t^{-5/3}$ power law decline while the late-time data can be fit by a $t^{-5/12}$ decline, indicating we may be seeing a transition from a fallback-dominated emission regime to a disk-dominated regime. Finally, the blackbody radius associated with the UV and optical emission is orders of magnitude larger than that of the thermal X-rays, indicating that the two types of radiation are likely coming from different regions around the SMBH.

ASASSN-15oi provides another piece of evidence that detailed late-time observations of TDEs are necessary to fully characterize the emission of these rare transients. Very little evolution was seen in the X-ray emission at early times, but the late-time observations showed that ASASSN-15oi exhibited unique evolution that may help shed light on the

physical processes responsible for this emission. Further, while the spectral features faded rapidly in ASASSN-15oi, it continued to exhibit UV emission for hundreds of days after discovery, indicating again that transient TDE emission can contaminate host galaxies for years following a tidal disruption. The late-time UV observations are once again able to rule out a purely $t^{-5/3}$ decline in the luminosity, indicating that the evolution of the luminosity associated with TDEs is more complex than simple theoretical models. Continued study of ASASSN-15oi will help shed light on the nature of the non-thermal X-ray emission, and future TDE discoveries should be observed for similarly long periods of time in order to fully characterize the emission from these events and allow us to more accurately model the physical processes responsible.

ACKNOWLEDGMENTS

The authors thank K. Stanek, E. Ramirez-Ruiz, and B. Mockler for their suggestions and comments for improving the manuscript. We thank N. Morrell for obtaining follow-up observations. We thank Las Cumbres Observatory and its staff for their continued support of ASAS-SN.

ASAS-SN is supported by NSF grant AST-1515927. Development of ASAS-SN has been supported by NSF grant AST-0908816, the Center for Cosmology and AstroParticle Physics at the Ohio State University, the Mt. Cuba Astronomical Foundation, and by George Skestos.

CSK is supported by NSF grant AST-1515876. Support for JLP is in part provided by the Ministry of Economy, Development, and Tourism's Millennium Science Initiative through grant IC120009, awarded to The Millennium Institute of Astrophysics, MAS.

This research has made use of the XRT Data Analysis Software (XRTDAS) developed under the responsibility of the ASI Science Data Center (ASDC), Italy. At Penn State the NASA *Swift* program is support through contract NAS5-00136.

This research was made possible through the use of the AAVSO Photometric All-Sky Survey (APASS), funded by the Robert Martin Ayers Sciences Fund.

This research has made use of data provided by Astrometry.net (Barron et al. 2008).

This paper uses data products produced by the OIR Telescope Data Center, supported by the Smithsonian Astrophysical Observatory.

This publication makes use of data products from the Two Micron All Sky Survey, which is a joint project of the University of Massachusetts and the Infrared Processing and Analysis Center/California Institute of Technology, funded by the National Aeronautics and Space Administration and the National Science Foundation.

This publication makes use of data products from the Wide-field Infrared Survey Explorer, which is a joint project of the University of California, Los Angeles, and the Jet Propulsion Laboratory/California Institute of Technology, funded by the National Aeronautics and Space Administration.

This research has made use of the NASA/IPAC Extragalactic Database (NED), which is operated by the Jet Propulsion Laboratory, California Institute of Technology,

under contract with the National Aeronautics and Space Administration.

This work is based in part on observations collected at the European Organisation for Astronomical Research in the Southern Hemisphere, Chile as part of PESSTO, (the Public ESO Spectroscopic Survey for Transient Objects Survey) ESO program 188.D-3003, 191.D-0935.

This publication makes use of data obtained from the Weizmann interactive supernova data repository (WISE-ERP; Yaron & Gal-Yam 2012).

REFERENCES

- Arcavi I. et al., 2014, *ApJ*, 793, 38
 Assef R. J. et al., 2013, *ApJ*, 772, 26
 Auchettl K., Guillochon J., Ramirez-Ruiz E., 2017, *ApJ*, 838, 149
 Auchettl K., Ramirez-Ruiz E., Guillochon J., 2018, *ApJ*, 852, 37
 Barron J. T., Stumm C., Hogg D. W., Lang D., Roweis S., 2008, *AJ*, 135, 414
 Blagorodnova N. et al., 2017, *ApJ*, 844, 46
 Breeveld A. A. et al., 2010, *MNRAS*, 406, 1687
 Brimacombe J. et al., 2015, *The Astronomer's Telegram*, 7910, 1
 Brown J. S., Holoién T. W.-S., Auchettl K., Stanek K. Z., Kochanek C. S., Shappee B. J., Prieto J. L., Grupe D., 2017, *MNRAS*, 466, 4904
 Brown J. S. et al., 2018, *MNRAS*, 473, 1130
 Brown J. S., Shappee B. J., Holoién T. W.-S., Stanek K. Z., Kochanek C. S., Prieto J. L., 2016, *MNRAS*, 462, 3993
 Bruzual G., Charlot S., 2003, *MNRAS*, 344, 1000
 Burrows D. N. et al., 2005, *SSR*, 120, 165
 Cardelli J. A., Clayton G. C., Mathis J. S., 1989, *ApJ*, 345, 245
 Cenko S. B. et al., 2012, *MNRAS*, 420, 2684
 Chambers K. C. et al., 2016, *ArXiv e-prints*
 Chornock R. et al., 2014, *ApJ*, 780, 44
 Dressler A. et al., 2011, *PASP*, 123, 288
 Evans C. R., Kochanek C. S., 1989, *ApJ*, 346, L13
 Flewelling H. A. et al., 2016, *ArXiv e-prints*
 Gaskell C. M., Rojas Lobos P. A., 2014, *MNRAS*, 438, L36
 Gezari S., Cenko S. B., Arcavi I., 2017, *ApJ*, 851, L47
 Gezari S., Chornock R., Lawrence A., Rest A., Jones D. O., Berger E., Challis P. M., Narayan G., 2015, *ApJ*, 815, L5
 Gezari S. et al., 2012, *Nature*, 485, 217
 Guillochon J., Nicholl M., Villar V. A., Mockler B., Narayan G., Mandel K. S., Berger E., Williams P. K. G., 2017, *MOSFIT: Modular Open-Source Fitter for Transients. Astrophysics Source Code Library*
 Guillochon J., Ramirez-Ruiz E., 2013, *ApJ*, 767, 25
 Hayasaki K., Stone N., Loeb A., 2013, *MNRAS*, 434, 909
 Hayasaki K., Stone N., Loeb A., 2016, *MNRAS*, 461, 3760
 Holoién T. W.-S. et al., 2016a, *MNRAS*, 463, 3813
 Holoién T. W.-S. et al., 2016b, *MNRAS*, 455, 2918
 Holoién T. W.-S. et al., 2014, *MNRAS*, 445, 3263
 Hung T. et al., 2017, *ApJ*, 842, 29
 Kalberla P. M. W., Burton W. B., Hartmann D., Arnal E. M., Bajaja E., Morras R., Pöppel W. G. L., 2005, *A&A*, 440, 775
 Kochanek C. S., 1994, *ApJ*, 422, 508
 Kochanek C. S., 2016, *MNRAS*, 461, 371
 Kriek M., van Dokkum P. G., Labbé I., Franx M., Illingworth G. D., Marchesini D., Quadri R. F., 2009, *ApJ*, 700, 221
 Liu T. et al., 2017, *ApJS*, 232, 8
 Lodato G., Rossi E. M., 2011, *MNRAS*, 410, 359
 MacLeod C. L. et al., 2012, *ApJ*, 753, 106
 Mangan V., Burrows D. N., Sbarufatti B., Cannizzo J. K., 2016, *ApJ*, 817, 103
 Marchesi S. et al., 2016, *ApJ*, 830, 100
 McConnell N. J., Ma C.-P., 2013, *ApJ*, 764, 184

- Metzger B. D., Stone N. C., 2016, MNRAS, 461, 948
Mockler B., Guillochon J., Ramirez-Ruiz E., 2018, ArXiv e-prints
Moretti A. et al., 2004, in Proc. SPIE, Vol. 5165, X-Ray and
Gamma-Ray Instrumentation for Astronomy XIII, Flanagan
K. A., Siegmund O. H. W., eds., pp. 232–240
Phinney E. S., 1989, Nature, 340, 595
Piran T., Svirski G., Krolik J., Cheng R. M., Shiokawa H., 2015,
ApJ, 806, 164
Poole T. S. et al., 2008, MNRAS, 383, 627
Rees M. J., 1988, Nature, 333, 523
Reines A. E., Volonteri M., 2015, ApJ, 813, 82
Ricci C. et al., 2017, ApJS, 233, 17
Roming P. W. A. et al., 2005, SSR, 120, 95
Roth N., Kasen D., 2018, ApJ, 855, 54
Roth N., Kasen D., Guillochon J., Ramirez-Ruiz E., 2016, ApJ,
827, 3
Schlafly E. F., Finkbeiner D. P., 2011, ApJ, 737, 103
Shappee B. J. et al., 2014, ApJ, 788, 48
Shiokawa H., Krolik J. H., Cheng R. M., Piran T., Noble S. C.,
2015, ApJ, 804, 85
Skrutskie M. F. et al., 2006, AJ, 131, 1163
Strubbe L. E., Murray N., 2015, MNRAS, 454, 2321
Strubbe L. E., Quataert E., 2009, MNRAS, 400, 2070
Tozzi P. et al., 2006, A&A, 451, 457
van Velzen S. et al., 2011, ApJ, 741, 73
Vinkó J. et al., 2015, ApJ, 798, 12
Voges W. et al., 1999, A&A, 349, 389
Wilms J., Allen A., McCray R., 2000, ApJ, 542, 914
Wright E. L. et al., 2010, AJ, 140, 1868
Yaron O., Gal-Yam A., 2012, PASP, 124, 668

This paper has been typeset from a $\text{\TeX}/\text{\LaTeX}$ file prepared by the author.

APPENDIX A: FOLLOW-UP PHOTOMETRY

All UV and optical follow-up photometry are presented in Table A1 in the Vega system.

Table A1. Photometric data of ASASSN-15oi.

MJD	Magnitude	Filter	Telescope	MJD	Magnitude	Filter	Telescope
57249.532	15.45 0.129	I	LCO	57321.794	17.14 0.077	V	LCO
57252.002	15.54 0.158	I	LCO	57327.129	17.26 0.045	V	LCO
57256.428	15.46 0.133	I	LCO	57329.844	17.25 0.055	V	LCO
57258.008	15.43 0.143	I	LCO	57332.791	17.28 0.051	V	LCO
57262.251	15.34 0.193	I	LCO	57335.816	17.29 0.065	V	LCO
57264.083	15.83 0.150	I	LCO	57344.415	17.22 0.060	V	LCO
57268.052	15.72 0.129	I	LCO	57346.420	17.17 0.066	V	LCO
57269.908	15.71 0.133	I	LCO	57349.423	17.32 0.056	V	LCO
57271.882	15.70 0.143	I	LCO	57355.035	17.25 0.052	V	LCO
57273.924	15.80 0.148	I	LCO	57264.392	16.52 0.061	V	Swift
57276.874	15.80 0.142	I	LCO	57268.788	16.92 0.100	V	Swift
57279.895	15.81 0.140	I	LCO	57272.514	16.89 0.071	V	Swift
57282.476	15.85 0.133	I	LCO	57276.096	17.01 0.071	V	Swift
57291.383	15.98 0.154	I	LCO	57280.688	17.07 0.071	V	Swift
57294.522	15.99 0.141	I	LCO	57285.415	17.01 0.091	V	Swift
57299.495	15.80 0.139	I	LCO	57291.590	17.06 0.130	V	Swift
57302.481	15.95 0.200	I	LCO	57294.588	17.08 0.091	V	Swift
57304.921	15.86 0.262	I	LCO	57300.236	17.36 0.100	V	Swift
57307.106	15.93 0.126	I	LCO	57303.628	17.13 0.100	V	Swift
57307.140	15.96 0.125	I	LCO	57306.494	17.13 0.100	V	Swift
57316.018	15.98 0.134	I	LCO	57309.413	17.18 0.100	V	Swift
57319.059	16.05 0.152	I	LCO	57312.137	17.22 0.110	V	Swift
57321.796	16.04 0.116	I	LCO	57318.671	17.43 0.150	V	Swift
57327.133	16.03 0.126	I	LCO	57324.051	17.81 0.210	V	Swift
57329.849	15.88 0.128	I	LCO	57327.961	17.25 0.120	V	Swift
57332.796	16.02 0.159	I	LCO	57330.420	17.06 0.100	V	Swift
57335.821	16.06 0.157	I	LCO	57333.480	17.52 0.160	V	Swift
57346.424	15.83 0.140	I	LCO	57336.141	17.42 0.140	V	Swift
57349.419	15.87 0.133	I	LCO	57339.334	17.12 0.120	V	Swift
57355.039	15.92 0.121	I	LCO	57342.069	16.96 0.130	V	Swift
57249.533	16.01 0.053	V	LCO	57345.793	17.15 0.160	V	Swift
57252.004	16.06 0.055	V	LCO	57348.384	17.39 0.140	V	Swift
57256.429	16.10 0.053	V	LCO	57468.704	17.13 0.110	V	Swift
57258.009	16.30 0.225	V	LCO	57476.354	17.14 0.110	V	Swift
57259.334	16.20 0.051	V	Swift	57506.200	17.23 0.100	V	Swift
57262.252	16.52 0.144	V	LCO	57533.509	17.16 0.190	V	Swift
57266.065	16.55 0.112	V	LCO	57558.821	17.35 0.110	V	Swift
57268.053	16.63 0.047	V	LCO	57572.057	17.31 0.130	V	Swift
57269.909	16.76 0.050	V	LCO	57580.496	17.24 0.120	V	Swift
57271.883	16.79 0.062	V	LCO	57586.741	17.41 0.120	V	Swift
57273.926	16.83 0.058	V	LCO	57593.652	17.41 0.120	V	Swift
57276.875	16.93 0.057	V	LCO	57600.036	17.56 0.130	V	Swift
57278.172	16.94 0.062	V	LCO	57607.674	17.32 0.180	V	Swift
57282.475	16.98 0.050	V	LCO	57610.592	17.41 0.300	V	Swift
57285.424	16.90 0.130	V	LCO	57611.184	17.20 0.200	V	Swift
57291.382	17.03 0.081	V	LCO	57249.531	16.09 0.055	B	LCO
57294.521	17.13 0.074	V	LCO	57252.001	16.20 0.075	B	LCO
57304.919	17.22 0.074	V	LCO	57256.426	16.34 0.042	B	LCO
57307.104	17.18 0.047	V	LCO	57258.007	16.44 0.065	B	LCO
57307.138	17.18 0.056	V	LCO	57262.250	16.52 0.082	B	LCO
57312.170	17.20 0.068	V	LCO	57264.081	16.58 0.062	B	LCO
57315.877	17.28 0.082	V	LCO	57266.062	16.87 0.063	B	LCO
57315.894	17.14 0.073	V	LCO	57268.051	16.99 0.068	B	LCO
57316.016	17.24 0.075	V	LCO	57269.906	17.05 0.060	B	LCO
57319.057	17.23 0.059	V	LCO	57271.880	17.19 0.074	B	LCO

MJD	Magnitude	Filter	Telescope	MJD	Magnitude	Filter	Telescope
57273.923	17.38 0.067	<i>B</i>	LCO	57580.493	18.31 0.122	<i>B</i>	<i>Swift</i>
57276.872	17.26 0.069	<i>B</i>	LCO	57586.737	18.17 0.102	<i>B</i>	<i>Swift</i>
57278.169	17.42 0.076	<i>B</i>	LCO	57593.648	18.28 0.102	<i>B</i>	<i>Swift</i>
57282.474	17.47 0.065	<i>B</i>	LCO	57600.033	18.16 0.102	<i>B</i>	<i>Swift</i>
57285.423	17.62 0.083	<i>B</i>	LCO	57607.671	18.23 0.161	<i>B</i>	<i>Swift</i>
57291.381	17.70 0.115	<i>B</i>	LCO	57610.590	18.61 0.312	<i>B</i>	<i>Swift</i>
57294.520	17.58 0.242	<i>B</i>	LCO	57611.181	18.20 0.181	<i>B</i>	<i>Swift</i>
57295.130	17.67 0.085	<i>B</i>	LCO	57259.328	15.43 0.036	<i>U</i>	<i>Swift</i>
57299.493	17.95 0.098	<i>B</i>	LCO	57264.383	15.87 0.036	<i>U</i>	<i>Swift</i>
57304.918	17.59 0.086	<i>B</i>	LCO	57268.722	16.19 0.046	<i>U</i>	<i>Swift</i>
57307.137	17.93 0.067	<i>B</i>	LCO	57272.506	16.38 0.045	<i>U</i>	<i>Swift</i>
57312.168	17.98 0.077	<i>B</i>	LCO	57276.088	16.60 0.045	<i>U</i>	<i>Swift</i>
57315.873	18.27 0.130	<i>B</i>	LCO	57280.678	16.84 0.054	<i>U</i>	<i>Swift</i>
57315.891	18.09 0.122	<i>B</i>	LCO	57285.412	16.92 0.063	<i>U</i>	<i>Swift</i>
57316.015	18.09 0.086	<i>B</i>	LCO	57291.387	17.04 0.063	<i>U</i>	<i>Swift</i>
57319.055	18.21 0.108	<i>B</i>	LCO	57294.581	17.27 0.073	<i>U</i>	<i>Swift</i>
57321.792	18.45 0.179	<i>B</i>	LCO	57300.229	17.43 0.082	<i>U</i>	<i>Swift</i>
57327.124	18.12 0.058	<i>B</i>	LCO	57303.621	17.38 0.082	<i>U</i>	<i>Swift</i>
57329.839	18.14 0.049	<i>B</i>	LCO	57306.486	17.49 0.082	<i>U</i>	<i>Swift</i>
57332.786	18.31 0.099	<i>B</i>	LCO	57309.408	17.62 0.092	<i>U</i>	<i>Swift</i>
57335.812	18.18 0.102	<i>B</i>	LCO	57312.131	17.68 0.112	<i>U</i>	<i>Swift</i>
57344.411	18.25 0.077	<i>B</i>	LCO	57318.667	17.65 0.092	<i>U</i>	<i>Swift</i>
57346.415	18.11 0.131	<i>B</i>	LCO	57324.048	17.87 0.151	<i>U</i>	<i>Swift</i>
57349.414	18.27 0.076	<i>B</i>	LCO	57327.910	17.68 0.102	<i>U</i>	<i>Swift</i>
57353.420	18.24 0.064	<i>B</i>	LCO	57330.418	17.86 0.122	<i>U</i>	<i>Swift</i>
57355.030	18.35 0.071	<i>B</i>	LCO	57333.413	17.92 0.122	<i>U</i>	<i>Swift</i>
57259.329	16.38 0.036	<i>B</i>	<i>Swift</i>	57336.134	17.67 0.122	<i>U</i>	<i>Swift</i>
57264.384	16.75 0.045	<i>B</i>	<i>Swift</i>	57339.331	18.10 0.152	<i>U</i>	<i>Swift</i>
57268.724	16.94 0.045	<i>B</i>	<i>Swift</i>	57342.066	17.93 0.162	<i>U</i>	<i>Swift</i>
57272.507	17.20 0.045	<i>B</i>	<i>Swift</i>	57345.787	18.08 0.202	<i>U</i>	<i>Swift</i>
57276.089	17.31 0.054	<i>B</i>	<i>Swift</i>	57348.377	18.02 0.141	<i>U</i>	<i>Swift</i>
57280.679	17.43 0.054	<i>B</i>	<i>Swift</i>	57468.701	18.64 0.215	<i>U</i>	<i>Swift</i>
57285.413	17.55 0.063	<i>B</i>	<i>Swift</i>	57476.350	18.59 0.194	<i>U</i>	<i>Swift</i>
57291.388	17.64 0.063	<i>B</i>	<i>Swift</i>	57506.198	18.44 0.142	<i>U</i>	<i>Swift</i>
57294.582	17.77 0.073	<i>B</i>	<i>Swift</i>	57533.506	18.54 0.305	<i>U</i>	<i>Swift</i>
57300.230	17.80 0.073	<i>B</i>	<i>Swift</i>	57558.815	18.50 0.152	<i>U</i>	<i>Swift</i>
57303.622	17.83 0.082	<i>B</i>	<i>Swift</i>	57572.053	18.22 0.162	<i>U</i>	<i>Swift</i>
57306.487	17.75 0.073	<i>B</i>	<i>Swift</i>	57580.493	18.56 0.203	<i>U</i>	<i>Swift</i>
57309.409	17.90 0.082	<i>B</i>	<i>Swift</i>	57586.736	18.95 0.235	<i>U</i>	<i>Swift</i>
57312.132	17.75 0.082	<i>B</i>	<i>Swift</i>	57593.648	18.53 0.162	<i>U</i>	<i>Swift</i>
57318.668	18.00 0.092	<i>B</i>	<i>Swift</i>	57600.033	18.8 0.213	<i>U</i>	<i>Swift</i>
57324.049	18.10 0.132	<i>B</i>	<i>Swift</i>	57607.670	18.18 0.212	<i>U</i>	<i>Swift</i>
57327.911	18.04 0.092	<i>B</i>	<i>Swift</i>	57610.590	>18.45	<i>U</i>	<i>Swift</i>
57330.418	18.00 0.102	<i>B</i>	<i>Swift</i>	57611.181	18.25 0.273	<i>U</i>	<i>Swift</i>
57333.414	18.05 0.102	<i>B</i>	<i>Swift</i>	57259.325	14.62 0.042	<i>W1</i>	<i>Swift</i>
57336.135	18.13 0.132	<i>B</i>	<i>Swift</i>	57264.379	15.00 0.042	<i>W1</i>	<i>Swift</i>
57339.332	18.23 0.132	<i>B</i>	<i>Swift</i>	57268.719	15.31 0.042	<i>W1</i>	<i>Swift</i>
57342.066	17.98 0.132	<i>B</i>	<i>Swift</i>	57272.503	15.53 0.042	<i>W1</i>	<i>Swift</i>
57345.788	18.26 0.171	<i>B</i>	<i>Swift</i>	57276.085	15.84 0.042	<i>W1</i>	<i>Swift</i>
57348.378	18.36 0.141	<i>B</i>	<i>Swift</i>	57280.675	16.06 0.05	<i>W1</i>	<i>Swift</i>
57468.701	18.23 0.122	<i>B</i>	<i>Swift</i>	57285.411	16.27 0.05	<i>W1</i>	<i>Swift</i>
57476.350	18.40 0.122	<i>B</i>	<i>Swift</i>	57291.384	16.53 0.05	<i>W1</i>	<i>Swift</i>
57506.198	18.23 0.092	<i>B</i>	<i>Swift</i>	57294.579	16.64 0.058	<i>W1</i>	<i>Swift</i>
57533.506	18.12 0.161	<i>B</i>	<i>Swift</i>	57297.048	16.91 0.076	<i>W1</i>	<i>Swift</i>
57558.816	18.27 0.102	<i>B</i>	<i>Swift</i>	57300.226	16.92 0.058	<i>W1</i>	<i>Swift</i>
57572.054	18.53 0.151	<i>B</i>	<i>Swift</i>	57303.618	17.10 0.067	<i>W1</i>	<i>Swift</i>

MJD	Magnitude	Filter	Telescope	MJD	Magnitude	Filter	Telescope
57306.483	17.18 0.067	W1	Swift	57476.354	19.83 0.202	M2	Swift
57309.407	17.21 0.067	W1	Swift	57493.299	20.16 0.341	M2	Swift
57312.128	17.36 0.076	W1	Swift	57501.204	20.15 0.262	M2	Swift
57318.666	17.47 0.076	W1	Swift	57506.200	20.02 0.212	M2	Swift
57324.047	17.73 0.104	W1	Swift	57514.309	>19.87	M2	Swift
57327.909	17.84 0.085	W1	Swift	57521.082	20.27 0.321	M2	Swift
57330.416	17.67 0.085	W1	Swift	57528.985	19.94 0.272	M2	Swift
57333.412	17.90 0.095	W1	Swift	57533.510	>19.72	M2	Swift
57336.132	17.91 0.104	W1	Swift	57558.822	>20.72	M2	Swift
57339.330	17.88 0.104	W1	Swift	57572.057	>20.32	M2	Swift
57342.064	17.96 0.133	W1	Swift	57580.497	>20.39	M2	Swift
57345.784	18.25 0.173	W1	Swift	57586.741	>20.67	M2	Swift
57348.374	18.18 0.114	W1	Swift	57593.652	20.28 0.282	M2	Swift
57468.700	19.23 0.222	W1	Swift	57600.036	20.07 0.252	M2	Swift
57476.348	19.51 0.242	W1	Swift	57607.675	>19.37	M2	Swift
57493.302	19.32 0.202	W1	Swift	57610.592	>19.16	M2	Swift
57501.209	19.22 0.143	W1	Swift	57611.184	>19.63	M2	Swift
57506.197	19.50 0.212	W1	Swift	57257.794	14.78 0.036	W2	Swift
57514.700	19.37 0.232	W1	Swift	57259.330	14.81 0.042	W2	Swift
57521.086	19.15 0.153	W1	Swift	57264.386	15.13 0.042	W2	Swift
57528.989	19.50 0.182	W1	Swift	57268.725	15.28 0.042	W2	Swift
57533.504	19.20 0.341	W1	Swift	57272.508	15.48 0.042	W2	Swift
57558.812	19.37 0.212	W1	Swift	57276.091	15.67 0.042	W2	Swift
57572.051	19.71 0.361	W1	Swift	57280.681	15.87 0.042	W2	Swift
57580.491	19.78 0.361	W1	Swift	57285.413	15.98 0.042	W2	Swift
57586.735	19.36 0.222	W1	Swift	57291.389	16.14 0.042	W2	Swift
57593.646	19.67 0.262	W1	Swift	57294.583	16.16 0.042	W2	Swift
57600.031	19.37 0.222	W1	Swift	57300.231	16.38 0.050	W2	Swift
57607.668	>19.41	W1	Swift	57303.623	16.41 0.050	W2	Swift
57610.589	>18.84	W1	Swift	57306.488	16.59 0.050	W2	Swift
57611.179	>19.14	W1	Swift	57309.410	16.65 0.050	W2	Swift
57259.335	14.43 0.042	M2	Swift	57312.133	16.77 0.050	W2	Swift
57264.394	14.86 0.042	M2	Swift	57318.668	17.00 0.050	W2	Swift
57268.789	15.21 0.050	M2	Swift	57324.049	17.09 0.067	W2	Swift
57272.515	15.36 0.042	M2	Swift	57327.911	17.17 0.058	W2	Swift
57276.098	15.59 0.042	M2	Swift	57330.418	17.24 0.058	W2	Swift
57280.689	15.80 0.050	M2	Swift	57333.414	17.38 0.067	W2	Swift
57285.416	16.02 0.042	M2	Swift	57336.136	17.39 0.067	W2	Swift
57291.591	16.18 0.050	M2	Swift	57339.332	17.45 0.067	W2	Swift
57294.589	16.39 0.050	M2	Swift	57342.067	17.43 0.076	W2	Swift
57300.237	16.64 0.050	M2	Swift	57345.789	17.50 0.085	W2	Swift
57303.629	16.79 0.050	M2	Swift	57348.379	17.60 0.067	W2	Swift
57306.495	16.86 0.050	M2	Swift	57468.702	19.76 0.212	W2	Swift
57309.413	16.97 0.050	M2	Swift	57476.351	19.60 0.182	W2	Swift
57312.138	17.05 0.058	M2	Swift	57493.296	19.76 0.212	W2	Swift
57318.869	17.40 0.182	M2	Swift	57501.199	19.93 0.182	W2	Swift
57324.052	17.51 0.076	M2	Swift	57506.198	19.90 0.202	W2	Swift
57327.962	17.59 0.067	M2	Swift	57514.307	20.01 0.262	W2	Swift
57330.421	17.71 0.067	M2	Swift	57521.079	20.07 0.232	W2	Swift
57333.481	17.85 0.076	M2	Swift	57528.257	20.02 0.232	W2	Swift
57336.142	17.85 0.076	M2	Swift	57533.507	>19.75	W2	Swift
57339.334	17.95 0.076	M2	Swift	57558.817	20.04 0.222	W2	Swift
57342.069	17.88 0.095	M2	Swift	57572.054	20.20 0.331	W2	Swift
57345.794	17.94 0.242	M2	Swift	57580.494	20.20 0.311	W2	Swift
57348.385	17.93 0.076	M2	Swift	57586.738	19.68 0.192	W2	Swift
57468.704	19.70 0.192	M2	Swift	57593.649	20.23 0.272	W2	Swift

MJD	Magnitude	Filter	Telescope	MJD	Magnitude	Filter	Telescope
57600.034	20.33 0.341	W2	<i>Swift</i>	57611.182	>19.66	W2	<i>Swift</i>
57607.671	>19.92	W2	<i>Swift</i>	57833.642	>20.36	W2	<i>Swift</i>
57610.590	>19.41	W2	<i>Swift</i>	57845.002	20.27 0.163	W2	<i>Swift</i>

All magnitudes and uncertainties are presented in the Vega system. Uncertainties are given next to the magnitude measurements, except for upper limits. Data are not corrected for Galactic extinction. The abbreviation “LCO” refers to the Las Cumbres Observatory telescopes.